In situ imaging of dealloying during nanoporous gold formation by transmission X-ray microscopy

Yu-chen Karen Chen-Wiegart [a,b,*], Steve Wang [b], Wah-Keat Lee [b], Ian McNulty [b], Peter W. Voorhees [a], David C. Dunand [a]

[a] *Department of Materials Science and Engineering, Northwestern University, Evanston, IL 60208, USA*
[b] *Advanced Photon Source, Argonne National Laboratory, Argonne, IL 60439, USA*

Abstract

The dealloying process is directly imaged, for the first time, by using transmission X-ray microscopy for the case of an Ag–30 at.% Au wire dealloyed under free corrosion in nitric acid. The propagation of a sharp dealloying front separating the alloy from nanoporous Au was observed by two-dimensional real-time *in situ* imaging at 30 nm resolution and measured in detail in three dimensions by an *ex situ* nanotomography technique at fixed time intervals. The rate of the dealloying front propagation is independent of the dealloying time up to a 3 μm depth, indicating that the dealloying process to this depth is dominated by interfacial effects (i.e. gold surface diffusion and/or silver dissolution) rather than long-range transport effects (i.e. diffusion of acid and corrosion product in and out of the porous layer). The constant dealloying rate corresponds to a constant silver flux and a constant current density, even though the potential might be fluctuating under free corrosion conditions and the interfacial area is shrinking as a function of time. Free corrosion in this system generates a high current density, implying it is driven by a chemical potential difference that is much higher than the critical potential.
© 2012 Acta Materialia Inc. Published by Elsevier Ltd. All rights reserved.

Keywords: TXM; X-ray synchrotron radiation; Metal foam

1. Introduction

Dealloying is a simple processing method to fabricate nanoporous metallic structures. By dissolving the less noble component from a binary alloy, a nanoporous (np) structure of the more noble metal with open pores ranging from ~3 to 50 nm in size can be fabricated for various geometries (nanoscale wires, rods, spheres and core–shell structures, microscale thin films, and macroscale foils and foams) and various metals (Au, Ag, Fe, Co, Ni, Pd, Pt and Ti) [1–8]. Numerous applications – including sensors, actuators, super-capacitor, anodes of Li-ion battery and catalytic substrates – have been reported for np-metals [9–14]. Understanding the mechanism of dealloying is essential to optimize the process and fabricate structures with properties optimized for a particular application. In particular, with an accurate understanding of the variables controlling dealloying front propagation, nanoporous gold could be prepared with the shortest possible dealloying time, thus ensuring the highest possible specific area, since pore/ligament coarsening occurs in freshly dealloyed np-Au in the electrolyte [15,16]. This property affects sensitively the performance of catalysts, sensors, actuators, battery electrode and surface Raman scattering [9–14]. With the accurate measurement of dealloying rate provided here, it is also possible to fabricate partially dealloyed structures where the surface only is nanoporous, combining the functional properties of the dealloyed, nanoporous surface with the enhanced mechanical properties (in particular ductility and toughness) provided by the non-porous, non-dealloyed core of the material.

* Corresponding author. Present address: Photon Science, Brookhaven National Laboratory, Upton, NY 11973, USA. Tel.: +1 631 344 3463; fax: +1 631 344 3238.
  E-mail address: ycchen@bnl.gov (Yu-chen Karen Chen-Wiegart).

At steady state, dealloying consists of four steps [15,16]: (i) the electrolyte diffuses through the pores to supply the dissolving agent; (ii) the less noble component in the alloy reacts with, and dissolves into, the electrolyte; (iii) the dissolved ions diffuse out through the nanopores; and (iv) the noble component diffuses along the interface between the alloy and the electrolyte to further expose the less noble component in the alloy. Steps (i) and (iii) involve long-range diffusion or transport of electrolyte or ions, while steps (ii) and (iv) involve processes that take place along the pore–solid interface. A kinetic Monte Carlo simulation model has successfully reproduced the nanopore formation by only considering these two interface-controlled process [17]. Experimentally, it has been shown that a steady-state current develops during dealloying via electrochemical means and that this current changes as a function of applied potential, again indicating that an interface-control process might be the rate-determining mechanism in dealloying. [18].

However, interfacial control of the dealloying process has not been directly observed, to our knowledge. Furthermore, it is still a challenge to quantify the dealloying behavior as a function of dealloying time without applying an external voltage. It has been shown that, at a later stage, when most of the less-noble element has been dissolved, the pore size increases proportionally with the dealloying time raised to the power 1/4, which indicates that the process is governed by diffusion [19]. However, it is not clear whether this result is related to the dealloying process or whether coarsening of the porous structure occurs concurrently with dissolution. The concept of a "dealloying front" or "etching front" – the interface between the nanoporous structure and the alloy – has been widely adopted in the literature [20,21]. If propagation of the dealloying front can be imaged in a bulk alloy in situ and in real time, not only can the global dissolution rate be quantified, but also detailed local effects, such as the sample geometry, can be examined.

Here, we use real-time in situ transmission X-ray microscopy (TXM) to image a dealloying front to shed light on the underlying dealloying mechanism. By quantifying the dealloying front propagation velocity v_d as a function of time t, we obtain a direct measurement of the kinetics of dissolution and pore formation. Compared to electrochemical measurements [22–26], in which both the dissolution from the bulk alloy and the dissolution of residual silver from nanoporous gold contribute to the measured current density, imaging allows a direct quantitative measurement of the dealloying front position itself. The direct in situ imaging technique is more direct than measuring the evolution of the nanopore size, which combines effects of dealloying and coarsening [19]. From the in situ imaging data, we then determine the dealloying mechanism from the exponent of the power law relation between the dealloying time and the dealloying distance. Finally, the quantity of the residual silver in the nanoporous layer is determined, and the flux of silver is also calculated. A comparison of the flux of the silver measured from different methods is made by comparing direct imaging, electrochemical measurements and simulations.

2. Experimental procedures

Ag–30 at.% Au alloy wires with a diameter of 20–50 μm were fabricated by drawing the melted alloy within a Pyrex glass tube. Dealloying was carried out by immersing alloy samples in nitric acid (75% concentration, with assay 68–70 vol.%, or 11.7 M) without an applied voltage.

The TXM instrument located at beamline 32-ID-C at the Advanced Photon Source (Argonne National Laboratory, IL) [27] was used to measure the dealloying distance as a function of time by imaging the dealloying front in the Ag–30 at.% Au wires. TXM is a lens-based full-field imaging technique [27]. The objective lens used was a Fresnel zone plate, providing 30–40 nm resolution for two-dimensional projections [28]. All the images were taken at an X-ray energy of 10.4 keV, with an exposure time of 2 s. A lens-coupled scintillated CCD detector was used to record the images.

First, tomographic TXM of the dealloying process was conducted ex situ in Zernike phase contrast mode [29] to enhance the edge contrast along the porous/solid interface. An as-cast Ag–30 at.% Au tip was fractured from the wire while in the glass (sample A), creating a tapered tip with a roughly ellipsoidal cross-section and ~10 and ~15 μm axes. The tip was immersed in nitric acid for 30 s, then rinsed with deionized water before the TXM measurements. These procedures were repeated, resulting in an image series visualizing different stages of the process ex situ to quantitatively measure the dealloying behavior in three dimensions as a function of the dealloying time. For the reconstructions, a series of two-dimensional (2-D) projection images was collected over a 180° angular range with 0.5° increments. The 2-D projections were used to create a 3-D reconstruction using a filtered back-projection algorithm [30].

Dynamic in situ dealloying experiments were conducted to study the dealloying process without interruptions, first with an as-cast fracture tip (sample B) similar to sample A and with ~10 and ~15 μm dimensions, and second with three samples (samples C, D and E) shaped by focused ion beam milling (FIB) into 16 μm diameter cylinders. The FIB samples provided a regular sample geometry to accurately quantify the dealloying rate. The in situ dealloying cell (Fig. 1(a)) consisted of a Kapton capillary with a 0.5 mm inner diameter surrounding the silver–gold alloy tip. The capillary was nearly transparent to the 10.4 keV X-rays and contained nitric acid. A syringe inserted in the top of the capillary was triggered by a motorized controller, creating a continuous flow of acid during the X-ray imaging process. Samples C–E were imaged at different locations of two FIB tips – for C, at the top of the cylinder, and for D and E, away (by ~40 μm) from the top (Fig. 1(b)) – in order to compare edge effects on the reaction. Absorption contrast, rather than Zernike phase contrast, was used in the
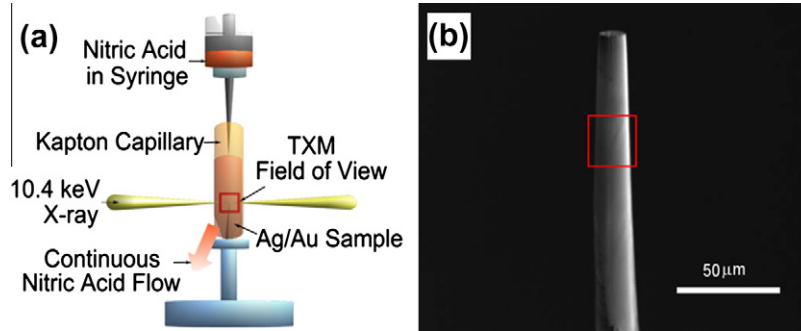
Fig. 1. (a) Schematic drawing of the experimental set-up for *in situ* dealloying experiment. (b) Scanning electron micrograph of sample D before dealloying, prepared by FIB. The field of view in TXM is 24 μm, marked with a rectangle.

experiments with the FIB sample, to enable quantitative analysis of the images.

3. Results and discussion

3.1. Ex situ imaging of dealloying front propagation

The dealloying front between the dealloyed region (np-Au) and the non-dealloyed region (Ag–30 at.% Au alloy) was clearly visible in the *ex situ* experiment from the relative X-ray attenuation differences of the two materials. Fig. 2 shows a tomographic reconstruction of the partially dealloyed tip of sample A after 90 s of dealloying. The shape of the sample is irregular because it was fractured from the wire while in the glass, as described above. Fig. 3 presents 2-D projections and 3-D reconstructed cross-sections, which show the dealloying front propagation as a function of dealloying time. A detailed procedure describing the general method used in this paper to quantify the dealloying distance can be found in Supplemental Fig. 1. The dealloying front did not advance during the tomography measurement, confirming that the deionized water rinse was an effective way to stop the dealloying process. The 3-D reconstruction further shows the sharp boundary across the np-Au/Ag–Au interface. The propagation of the dealloying front appears to be planar, so that

the overall sample geometry is preserved. This knowledge about the sample geometry preservation is critical as it allows the use of the 2-D projections in the *in situ* experiment to characterize the propagation rate of the dealloying front. In addition, it is demonstrated here that, using TXM, the dealloying front can be visualized and its propagation distance can be quantified in the *in situ* experiment because there is sufficient contrast between the dealloyed nanoporous region and the alloyed Ag–Au core.

3.2. In situ imaging of dealloying front propagation

3.2.1. Dealloying front propagation rate

Selected projections captured during the *in situ* dealloying experiments are shown in Figs. 4–7 for the non-FIB (sample B), FIB tip (sample C) and FIB center (sample D) samples, respectively. Movies from these *in situ* imaging experiments, using all projections captured, are available as Supplementary material online.

In Fig. 4, sample B shows the same dealloying behavior as sample A in the *ex situ* dealloying experiment. However, the total time to propagate the dealloying front into the center of the sample, as measured 15 μm from the tip, is more (~180 s for sample A vs. 300 s for sample B). This discrepancy may be due to the finite time it takes to stop the dissolution during the water rinse process. The quantitative

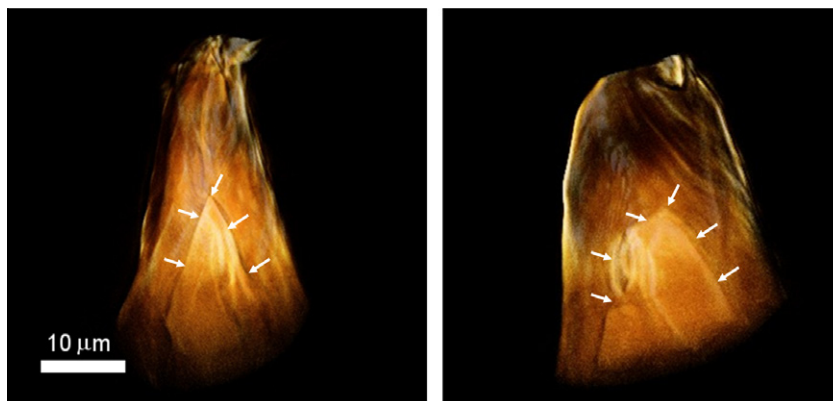Fig. 2. Tomographic reconstruction (volume rendering) of partially dealloyed sample A (90 s) from two different angles, rotated by 90°. The dealloying front is highlighted with arrows.
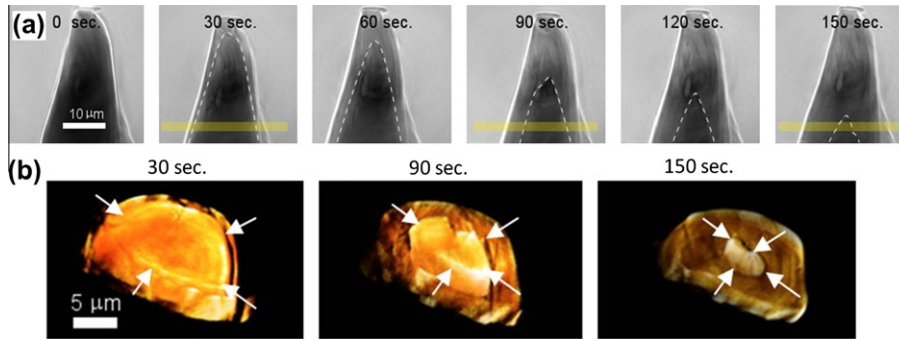
Fig. 3. (a) Series of X-ray transmission images showing the dealloying front propagation with *ex situ* imaging (sample A). The dealloying front is highlighted with a dashed line. (b) Cross-section of tomographic reconstruction of the selected volume marked in yellow in (a); the dealloying front is highlighted with arrows. (For interpretation of the references to colour in this figure legend, the reader is referred to the web version of this article.)
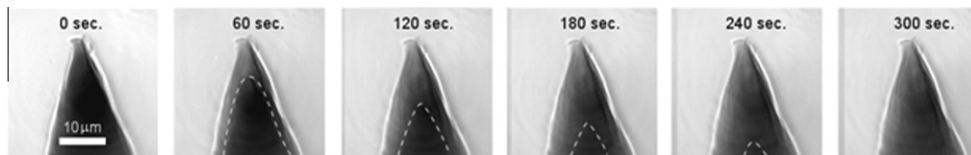

Fig. 4. Series of X-ray transmission images during dealloying of the non-FIB sample (sample B). Dashed lines represent the approximate position of the dealloying front.
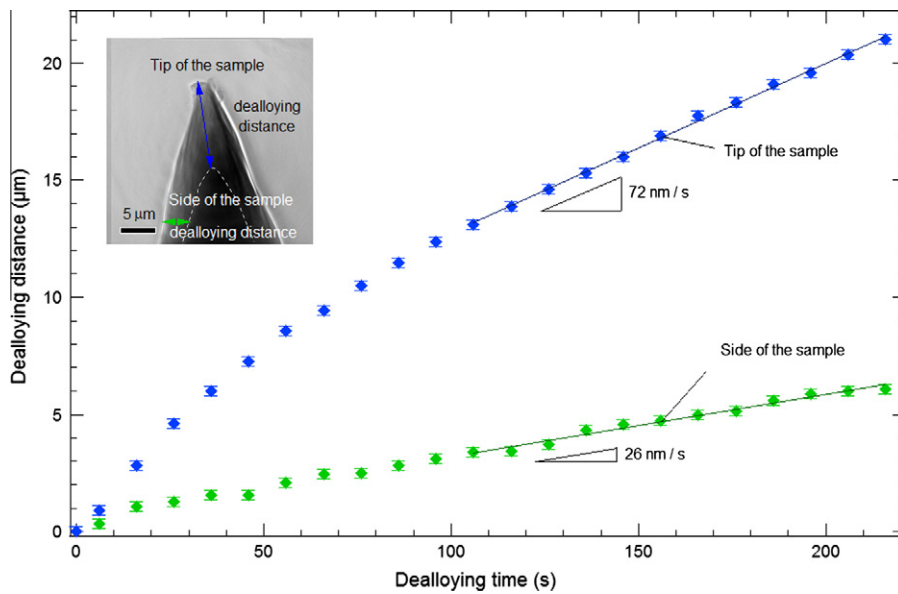

Fig. 5. Dealloying distance vs. time for sample B at the tip and side of the sample, with the two dealloying distances shown by arrows in the inset after 120 s of dealloying. The error bars are estimated based on the phase effect, which enhanced and blurred the interface.
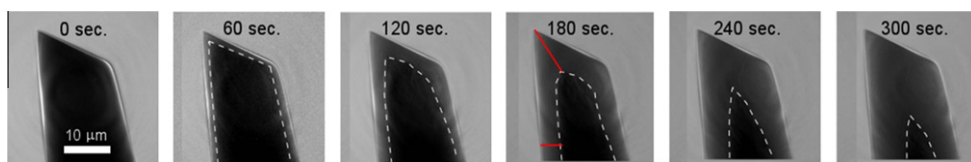

Fig. 6. Series of X-ray transmission images during dealloying imaged near the tip of FIB sample C. Dashed lines indicate the position of the dealloying front. Quantitative analysis of the dealloying rate in 180 s was carried out at the location marked as red lines. (For interpretation of the references to colour in this figure legend, the reader is referred to the web version of this article.)

results are shown in Fig. 5, in which the dealloying rate is about three times faster at the tip of the sample than at the side of the sample (72 vs. 26 nm s^{-1}). This can be due to either more rapid transport near the tip (due to the enhanced access to the acid from geometrical effects) if the process is long-range transport controlled or to the curvature effect (i.e. the Gibbs–Thompson effect [31]) if the process is interface controlled.

The dealloying behavior of the FIB sample near the tip (sample C, Fig. 6) is qualitatively similar to the non-FIB sample B, indicating that any surface modification that may have been produced by the FIB process does not affect the dealloying kinetics. A difference in the dealloying rate between the top and the side of the cylinder is still visible in Fig. 6, where the dissolution rates are linear and equal to 17 and 51 nm s^{-1} (see Supplemental information), for the side and the tip of the sample marked in Fig. 6, respectively. Compared to sample B, which has dealloying rates of 26 (side) and 72 nm s^{-1} (tip), these dealloying rates show reasonable reproducibility despite the different shapes in the samples. To avoid the above geometrical effect(s), only analysis of the dealloying of the FIB samples D and E, imaged far from the cylinder tip, was carried out. Fig. 7 shows a series of TXM *in situ* images during dealloying of sample D. The dealloying front does not advance uniformly for dealloying times longer than 200 s. A clear tip effect is visible at 240 s, as shown in the figure. In addition, the dealloying front is not completely planar during the first 200 s, which may be due to defects, such as small voids or surface roughness, pre-existing in the sample. These defects can locally enhance the dealloying process, thus locally disrupting the planarity of the front.

The dealloying front distance as a function of dealloying time was quantified by analyzing the images of the *in situ* dealloying of the FIB samples (samples D and E) with images taken away (40 μm) from the tip of the sample. Before the tip shape affected the dealloying front propagation behavior (i.e. for the first ~200 s), the dealloying front and the sample surface were generally in parallel. The intensity profile of each individual image which corresponds to a specific dealloying time was plotted as a function of the position within the sample. Each intensity profile was averaged over a 1 μm height in the image (as shown in Fig. 7). The derivative of the intensity was then calculated to determine the positions of the Ag–Au/np Au interface and the acid/np-Au interface (sample surface) in the images. The difference between these two positions gives the dealloying distance for each of the 80 frames. The dealloying distance was determined at three different positions, 5 μm apart (Fig. 7). The average of the dealloying distance among the three plotted positions is plotted as a function of the dealloying time in Fig. 8. The error bars were defined as the maximum and minimum values of the dealloying distance from the three positions. No data were plotted before 20 s of dealloying time for sample D and before 50 s for sample E because the sample surface and the dealloying front were too close to be differentiated in

the X-ray transmission images. No data were plotted after 180 s for sample D and 138 s for sample E because the tip shape affected the dissolution, as visible in Fig. 7.

It is evident from Fig. 8 that the data are fitted well with a linear function. The slope gives the dealloying front propagation rate v_d. For sample D, v_d is 16.6 ± 0.1 nm s^{-1}, with a coefficient of determination (R^2) of 0.9988, and for sample E, v_d is 18.4 ± 0.2 nm s^{-1}, with an R^2 of 0.9813. This result shows good reproducibility among different samples. Since the data from sample D were measured from a wider range of dealloying distances and times, we analyzed sample D further.

The linear relationship in Fig. 8 indicates that dealloying, for the present conditions and for depths of up to 3 μm (much larger than the pore size, which is <10 nm [19]), is independent of the depth of the front. Thus, it appears that long-range diffusive transport in the liquid does not dominate and the interface moves at a rate controlled by interfacial processes. Such processes include the reaction of the silver in the alloy with the nitric acid and the gold surface diffusion that is necessary to expose the underlying Ag–30 at.% Au alloy. As shown in simulations [15], these two processes will reach a steady state after a certain dealloying time. Characterization of the sample feature size at much later time scales is probing only the coarsening of the porous structure occurring in the acid and thus does not shed light on the dealloying process and the initial pore formation [32].

To further distinguish whether the chemical reaction or gold surface determines the dealloying rate, different experimental parameters – e.g. temperature, alloy composition and acid concentration – will need to be studied in future experiments. The imaging method employed in this study can also be applied to other dealloying systems [3,33,34], with and without applied voltage (the latter by designing X-ray transparent electrochemical cells).

Finally, if the constant rate of dealloying is maintained over a depth of 10 μm, our results show that dealloying of a typical 20 μm diameter wire or 20 μm thick foil is completed within only tens of minutes rather than the few hours typically employed by most investigators. This is relevant for the design and fabrication of devices using np metals, because overexposure to the electrolyte during the dealloying process leads to coarsening of the nanopores [17].

3.2.2. Silver flux at the dealloying front

Knowing the dealloying front propagation rate v_d, the flux of silver J_{Ag} (defined as the mass of silver dissolved into the solution per unit area per unit time) can then be calculated by the following equation:

$$J_{Ag} = v_d \rho_{Ag}(V_{Ag\text{-alloy}} - V_{Ag\text{-NPG}}) \qquad (1)$$

where ρ_{Ag} is the density of silver, $V_{Ag\text{-alloy}}$ is the volume fraction of the silver in the alloy (0.70) and $V_{Ag\text{-NPG}}$ is the residual silver behind the dealloying front within the np-Au, which is ~0–10%, as shown later in Section 3.2.3.

Using Eq. (1) and a v_d of 16.6 (sample D), a value $J_{Ag} = 10\text{–}12\ \mu g\ s^{-1}\ cm^{-2}$ is determined.

A constant v_d value implies that the flux J_{Ag} and current density j (calculated in the following section) are also constant, which is unexpected for the present free-corrosion case, since the over-potential is expected to fluctuate over time [35]. Steady-state current behavior has been reported both in experiments [18] and also in a dynamic Monte Carlo simulation [15].

To compare the constant J_{Ag} reported here with the steady-state current reported elsewhere, J_{Ag} can be converted into the current density (j) using Faraday's Law:

$$j = JnF/M \tag{2}$$

where F is the Faraday constant, $n = 1$ (Ag is monovalent) and M is the atomic mass of Ag. The resulting current density is 9–11 mA cm^{-2}. Since it is very challenging to measure the current density directly under free corrosion conditions with conventional electrochemical methods, no current density of silver/gold alloy dissolved in nitric acid has been reported experimentally. However, we can still compare this current density with other systems in which np-Au has been fabricated. Dursun et al. [18] reported that, in dealloying Ag–30 at.% Au with perchloric acid, the steady-state current density and the applied voltage were positively correlated. Their data in the steady-state current density study investigated a constant applied voltage of up to 1.24 V, which resulted in a current density of $\sim$0.126 mA cm^{-2}. The current density is exponentially related to the applied voltage. For instance, under a standard polarization measurement with a scan rate of 3 mV s^{-1}, the density current reaches about 1 mA cm^{-2} at 1.4 V. The current density of dealloying in free corrosion reported here is at least 10 times higher. The very high associated dealloying rate typically results in a porous structure with fine pores and gold ligaments [17,19], which are desirable for applications due to the larger specific area [36].

The flux can also be expressed in atomic units as $J_{Ag\text{-atom}} = 6\text{–}7 \times 10^{16}$ atoms s^{-1} cm^{-2}, using the atomic weight of silver and the Avogadro constant. Dividing by the number of site per cm^2 at (1 1 1) planes for Ag, $\phi_{111} = 1.39 \times 10^{15}$ cm^{-2}, the atomic flux is then $J_{Ag(111)} = 43\text{–}50$ atom s^{-1} site^{-1}. Erlebacher [15] determined by simulation that, for Ag–25 at.% Au, the potential is between 1.15 and 1.25 eV for a flux on the order of 10–100 atom s^{-1} site^{-1}. The intrinsic critical potential is between 0.925 and 0.95 eV [15], above which dealloying can be sustained and generates a porous structure. The current density strongly depends on the alloy composition, and the relationship between the current density and the alloy composition is not necessarily linear. We therefore cannot directly compare our result with the simulated data due to the difference in composition between our *in situ* study and the simulation. However, the free corrosion of Ag–30 at.% Au in nitric acid generates a high current density, implying that the system is driven by a chemical potential difference that is much higher than the critical potential.

3.2.3. Residual silver in the dealloyed volume

The dealloying front can be directly imaged due to the different silver composition between the alloyed and dealloyed regions. Therefore, it is possible to quantify the amount of residual silver in the dealloyed region. Since the contrast is only based on the absorption of monochromatic X-ray radiation, the transmitted intensity follows Beer's law, $I(t) = I_0 \exp(-\mu t)$, where μ is the absorption coefficient and t is the effective thickness. The ratio between the measured transmitted intensity (I) and the incoming intensity (I_0) is then:

$$\frac{I}{I_0} = \exp(-\mu_{Ag}t_{Ag}) \cdot \exp(-\mu_{Au}t_{Au}) \cdot \exp(-\mu_{bkg}t_{bkg}) \tag{3}$$

in which the exponential term is decomposed into three separate terms which describe the contributions from the silver (Ag), the gold (Au) and the background (bkg), consisting of nitric acid, Kapton capillary and air.

By normalizing the background intensity to 100%, the effective silver thickness t_{Ag} can be calculated using the above equation. The effective gold thickness is $t_{Au} = t_T \cdot v_{Au}$, where $v_{Au} = 0.298$ is the gold volume fraction (equal within error to the gold atomic fraction) and t_T is the total sample thickness, calculated based on the beam position within the cylindrical sample. As a check, we also calculated the thickness profile from the image before the dealloying reaction, and found that it agrees with the thickness profile calculated from the perfect cylindrical shape, with chi-square (χ^2) = 0.03. Therefore, only $t_{Ag} = t_T \cdot v_{Ag}$ is an unknown parameter in Eq. (3), from which the volume fraction of residual silver v_{Ag} within the dealloyed region can be calculated.

We have accounted for the projection of the intensity through the cylindrical sample, i.e. as an average along the beam direction, under the approximation that the dealloying front propagates along all the radial directions towards the center of the sample at the same rate. We therefore assume a cylindrical shape to calculate the residual silver along the dealloying front propagating direction, which can be thought of as a cylindrical shell propagating inwards, given a cross-section within the sample as shown in the inset of Fig. 9. A more detailed description of this calculation can be found in Supplemental Fig. 3.

The calculated silver fraction in sample D is plotted as a function of distance from the center of the sample in Fig. 9 for two dealloying times, averaged for the three positions shown in Fig. 7. From Fig. 9, it appears that the residual silver behind the dealloying front varies between 0 and 10 at.%, i.e. the gold fraction is between 90 and 100%. More precise quantification was limited due to the strong phase effects at the sample surface (the interface between acid and np-Au) and the dealloying front (the interface between the dealloyed and alloyed regions). The resulting strong enhancement in contrast and reduction in the projected X-ray images at the interface causes artifacts in the quantification of residual silver near both interfaces. In Fig. 9, There is a region $\sim$4 μm deep ahead of the dealloying front
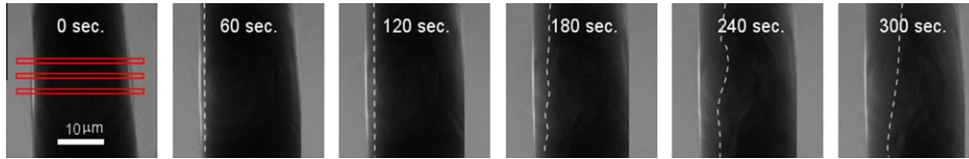
Fig. 7. Series of X-ray transmission images during dealloying, taken far from the tip of FIB sample D, with dashed lines as a guide to the eye to indicate the position of the dealloying front. Propagation of the dealloying front was only observed on the left side of the sample, because the right side of the sample drifted out of the field of view during the measurement (the bottom half of tip is truncated on the right, as indicated by the sharp vertical boundary). The dealloying kinetics at the three positions (marked as 1 μm thick line in figure) was analyzed.
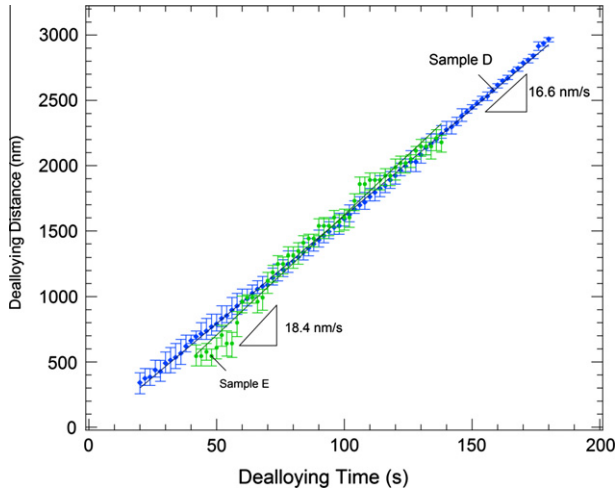
Fig. 8. Dealloying distance as a function of time in samples D and E.

that may appear to be a silver depleted region, but we believe this is an imaging phase-artifact since, at room temperature, silver has a diffusion length of 7×10^{-18} m for 150 s, as calculated using the diffusion coefficient of Ag in an Ag–35 at.% Au alloy, extrapolated to room temperature from a measurement temperature range of 630–1010 °C [37].

4. Conclusions

We observed the dealloying front propagation in an Ag–30 at.% Au alloy as a function of dealloying time using transmission X-ray microscopy using synchrotron X-rays. *Ex situ* nanotomography shows that the dealloying front propagates in three dimensions in a stable way that preserves the overall sample morphology. Two-dimensional imaging of the dealloying front propagation, carried out *in situ* and in real time, shows that the propagation rate of the dealloying front is remarkably constant, at 16–18 nm s^{-1}, over a 3 μm dealloying depth. The constant value indicates that (i) the dealloying process is interface controlled, i.e. it depends on the silver dissolution and/or the gold surface diffusion along the interface between the alloy and the np-Au; and (ii) the dealloying process is not controlled by the long-range diffusion or mass transport,
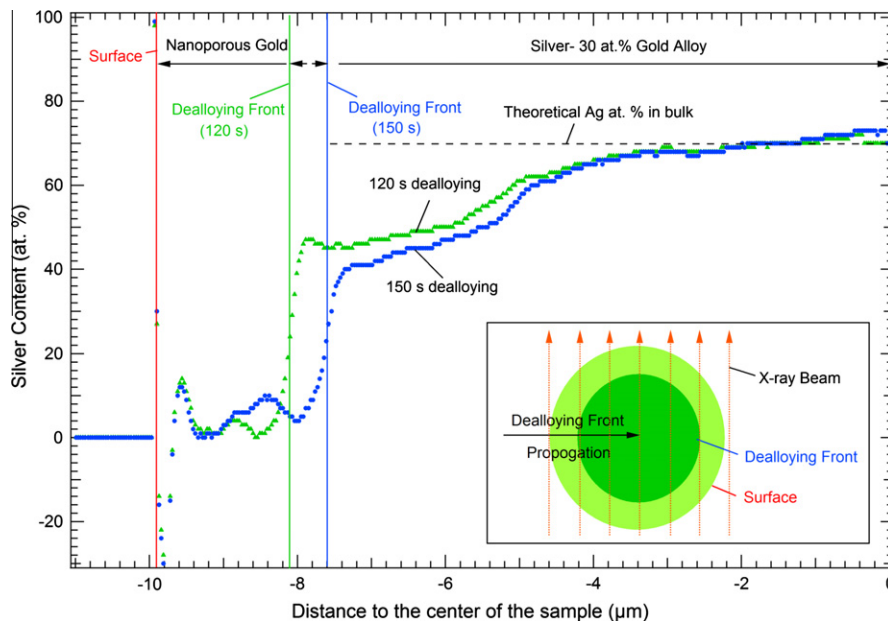

Fig. 9. Plot of silver content vs. radial distance from center of the sample at dealloying times of 120 and 150 s. The inset shows a schematic of a cross-section of sample D (∼16 μm in diameter) with beam positions. The strong phase effects at the interface caused artifacts and difficulties in quantifying the errors of the residual silver.

which includes the acid diffusing in – and/or the silver ions diffusing out – through the nanopores.

A sharp front represents a discontinuous transition of silver content and porosity, with 0–10 at.% residual silver in the dealloyed region. The constant front rate results in a constant silver flux and current density, despite the fact that the potential might be fluctuating under free corrosion conditions and the interfacial area is shrinking as a function of time. The high current density calculated from the measured flux also implies that a high chemical potential drives the process.

Acknowledgements

Appendix A. Supplementary material

Supplementary data associated with this article can be found, in the online version, at http://dx.doi.org/10.1016/j.actamat.2012.10.017.

References

[1] Cox ME, Dunand DC. Mater Sci Eng A-Struct Mater Properties Microstruct Process 2011;528:2401–6.
[2] Erlebacher J, Seshadri R. MRS Bull 2009;34:6.
[3] Li HQ, Misra A, Baldwin JK, Picraux ST. Appl Phys Lett 2009;95. 201902–1-3.
[4] Gu XH, Xu LQ, Tian F, Ding Y. Nano Res 2009;2:386–93.
[5] Dixon MC, Daniel TA, Hieda M, Smilgies DM, Chan MHW, Allara DL. Langmuir 2007;23:2414–22.
[6] Qian LH, Shen W, Shen B, Qin GWW, Das B. Nanotechnology 2010;21:7.
[7] Wada T, Yubuta K, Inoue A, Kato H. Mater Lett 2011;65:1076–8.
[8] Zhang Q, Wang XG, Qi Z, Wang Y, Zhang ZH. Electrochim Acta 2009;54:6190–8.
[9] Tappan BC, Steiner SA, Luther EP. Angew Chem-Int Ed 2010;49:4544–65.
[10] Ding Y, Chen M. MRS Bull 2009;34:8.
[11] Biener J, Wittstock A, Zepeda-Ruiz LA, Biener MM, Zielasek V, Kramer D, et al. Nat Mater 2009;8:47–51.
[12] Wittstock A, Zielasek V, Biener J, Friend CM, Baumer M. Science 2010;327:319–22.
[13] Yu Y, Gu L, Lang XY, Zhu CB, Fujita T, Chen MW, et al. Adv Mater 2011;23:2443.
[14] Lang X, Hirata A, Fujita T, Chen M. Nat Nanotechnol 2011;6:232–6.
[15] Erlebacher J. J Electrochem Soc 2004;151:C614–26.
[16] Erlebacher J, Aziz M, Karma A, Dimitrov N, Sieradzki K. Nature 2001;410:450–3.
[17] Ding Y, Kim YJ, Erlebacher J. Adv Mater 2004;16:1897–992.
[18] Dursun A, Pugh DB, Corcoran SG. J Electrochem Soc 2005;152:B65–72.
[19] Qian LH, Chen MW. Appl Phys Lett 2007;91. 083105–1-3.
[20] Kertis F, Snyder J, Govada L, Khurshid S, Chayen N, Erlebacher J. J Min Met Mater Soc 2010;62:50–6.
[21] Erlebacher J, Sieradzki K. Scripta Mater 2003;49:991–6.
[22] Pugh DV, Dursun A, Corcoran SG. J Electrochem Soc 2005;152:B455–9.
[23] Dursun A, Pugh DV, Corcoran SG. Electrochem Solid State Lett 2003;6:B32–4.
[24] Dursun A, Pugh DV, Corcoran SG. J Electrochem Soc 2003;150:B355–60.
[25] Pugh DV, Dursun A, Corcoran SG. J Mater Res 2003;18:216–21.
[26] Liu Y, Bliznakov S, Dimitrov N. J Electrochem Soc 2010;157:K168–76.
[27] Chen Y, Lo T, Chu Y, Yi J, Liu C, Wang J, et al. Nanotechnology 2008;19. 395302–1-5.
[28] Chu YS, Yi JM, De Carlo F, Shen Q, Lee WK, Wu HJ, et al. Appl Phys Lett 2008;92. 103119–1-3.
[29] Zernike F. Science 1955;121:345–9.
[30] Natterer F. The mathematics of computerized tomography. New York: Wiley; 1986.
[31] Balluffi RW, Allen SM, Carter WC. Kinetics of materials. New York: Wiley; 2005.
[32] Qian LH, Yan XQ, Fujita T, Inoue A, Chen MW. Appl Phys Lett 2007;90. 153120–1-3.
[33] Hakamada M, Mabuchi M. Mater Trans 2009;50:431–5.
[34] Qi Z, Zhao CC, Wang XG, Lin JK, Shao W, Zhang ZH, et al. J Phys Chem C 2009;113:6694–8.
[35] Jones D. Principles and prevention of corrosion. Englewood Cliffs, NJ: Prentice Hall; 1995.
[36] Qian LH, Inoue A, Chen MW. Appl Phys Lett 2008;92. 093113–1-3.
[37] Brandes EA, Brook GB. Smithell's metals reference book. 7 ed. Amsterdam: Elsevier; 1998.